Remote Sensing of Environment 145 (2014) 105–115

Contents lists available at ScienceDirect

Remote Sensing of Environment

journal homepage: www.elsevier.com/locate/rse

Turbid wakes associated with offshore wind turbines observed with Landsat 8

Quinten Vanhellemont *, Kevin Ruddick

Royal Belgian Institute for Natural Sciences (RBINS), Operational Directorate Natural Environment, 100 Gulledelle, 1200 Brussels, Belgium

ARTICLE INFO

Article history:
Received 14 November 2013
Received in revised form 17 January 2014
Accepted 18 January 2014
Available online 25 February 2014

Keywords:
Offshore wind farms
Turbid wakes
Suspended particulate matter
Landsat-8
Sensor noise
Spatial resolution

ABSTRACT

In the last decade, the number of offshore wind farms has increased rapidly. Offshore wind farms are typically constructed in near-shore, shallow waters. These waters can be highly productive or provide nursery grounds for fish. EU legislation requires assessment of the environmental impact of the wind farms. The effects on hard and soft substrate fauna, seabirds and marine mammals are most frequently considered. Here we present Landsat-8 imagery that reveals the impact of offshore wind farms on suspended sediments. Turbid wakes of individual turbines are observed that are aligned with tidal currents. They are 30–150 m wide, and several km in length. The environmental impact of these wakes and the source of the suspended material are still unclear, but the wake size warrants further study. The underwater light field will be affected by increased suspended sediments and the turbid wakes could significantly impact sediment transport and downstream sedimentation. The question of whether such features can be detected by other remote sensors is addressed by a theoretical analysis of the signal:noise specification for the Operational Land Imager (OLI), the Enhanced Thematic Mapper Plus (ETM+), the Advanced Very High Resolution Radiometer (AVHRR/3), the Moderate-Resolution Imaging Spectroradiometer (MODIS), the Spinning Enhanced Visible and Infrared Imager (SEVIRI), the Flexible Combined Imager (FCI) and the Multispectral Instrument (MSI) and by a demonstration of the impact of processing OLI data for different spatial resolutions.

1. Introduction

The first offshore wind farm was opened by Denmark in 1991, and consisted of 11 turbines with a combined capacity just under 5 MW (EWEA, 2011). For the next ten years, the construction of offshore wind farms was sporadic and limited to small-scale projects. After 2001, the installed capacity in Europe increased rapidly and by the end of 2012, 55 offshore wind farms were operational in Europe, with more than 1600 turbines and a total capacity just less than 5 GW, or 90% of the world total (EWEA, 2013). The United Kingdom had a 59% share in the European capacity, or over half of the world total, provided by 870 turbines on 20 farms (EWEA, 2013). This includes the two largest operational farms in the world: the London Array (630 MW) and the Greater Gabbard (504 MW). Both are located in the southern North Sea (SNS), as is in fact more than 40% of the world's offshore wind farm capacity: the combined nameplate capacity of seven farms in Belgian and UK waters is almost 2.2 GW (Table 1). There are currently five wind farms in and around the Thames estuary, two of which will be studied in more detail in this paper: the London Array and Thanet. Both have a large number of turbines supported by steel monopiles 4–7 m in diameter, piled up to 40 m in the seafloor (LORC, see reference in Table 1). In the EU, offshore wind farm projects are subject to the directives on Strategic Environmental Assessment (SEA, 2001/42/EC) and Environmental Impact Assessment (EIA, 85/337/EEC and amendments). Environmental surveying carried out before, during, and after construction allows for mitigation of adverse effects of wind farms.

Mapping of surface Suspended Particulate Matter concentration (SPM), also called Total Suspended Matter (TSM), has been routinely made using data from dedicated wide-swath ocean color instruments such as Orbview-2/SeaWiFS, Aqua/MODIS and ENVISAT/MERIS (e.g. Gohin, 2011; Nechad, Ruddick, & Park, 2010; Ouillon et al., 2008; Van der Woerd & Pasterkamp, 2004). These instruments offer a good compromise between revisit time (approx. daily at 50°N) and spatial resolution (ranging between 0.25 and 4 km). Marine reflectance in a single red channel can be used to reliably retrieve a wide range of SPM concentrations in the SNS (Nechad, Alvera-Azcaràte, Ruddick, & Greenwood, 2011; Vanhellemont, Greenwood & Ruddick, 2013). While few sensors are designed for ocean color, other satellite-borne passive optical instruments with a red and near-infrared channel have also been used for SPM mapping. Generally they have a lower quality than e.g. MODIS and MERIS, due to their lower signal-to-noise ratio, but are used when a higher spatial (e.g. Doxaran, Froidefond, Lavender, & Castaing, 2002; Mertes, Smith, & Adams, 1993) or temporal (Neukermans et al., 2009) resolution is required. Even before the ocean color era, passive imagers were used for turbidity mapping (e.g. Amos & Alföldi, 1979; Rouse &

* Corresponding author.
E-mail address: quinten.vanhellemont@mumm.ac.be (Q. Vanhellemont).

http://dx.doi.org/10.1016/j.rse.2014.01.009

Table 1
Seven wind farms in the southern North Sea, listed by nameplate capacity.
Source: Lindoe Offshore Renewables Centre, LORC, Offshore Wind Farms Map, http://www.lorc.dk/offshore-wind-farms-map/list, accessed 2013-10-14.

Name/phase (Country)	Coordinates	Capacity	Turbines	Depth	Installed
1. London Array/1 (UK)	51.63° N, 1.50° E	630 MW	175	0–25 m	2009–2013
2. Greater Gabbard (UK)	51.88° N, 1.94° E	504 MW	140	24–34 m	2009–2012
3. Thornton Bank/1 + 2 + 3 (BE)	51.55° N, 2.94° E	325 MW	54	12–28 m	2008–2013
4. Thanet (UK)	51.43° N, 1.63° E	300 MW	100	20–25 m	2009–2010
5. Gunfleet Sands (UK)	51.73° N, 1.24° E	172 MW	48	0–15 m	2008–2010
6. Belwind/1 (BE)	51.67° N, 2.80° E	165 MW	55	20–27 m	2009–2010
7. Kentish Flats/1 (UK)	51.46° N, 1.09° E	90 MW	30	5 m	2004–2005
Total		2186 MW	602		

Coleman, 1976; Stumpf & Pennock, 1989). The suitability of the Operational Land Imager on Landsat 8 (L8/OLI) for coastal zone monitoring has been demonstrated using simulated data (Gerace, Schott, & Nevins, 2013; Pahlevan & Schott, 2013).

On imagery with sufficient spatial resolution, large vessels and offshore constructions, such as wind turbines, can be easily distinguished (for example in Fig. 1), as they are highly reflective structures on a dark background (water). In the present study, imagery from Landsat 8 also reveals significant modification of near-surface suspended sediment concentration in the form of turbid wakes extending up to several km downstream of turbines installed offshore of the Thames estuary.

2. Methods

2.1. Study area

The southern North Sea (SNS) is a shallow sea (<50 m) with a sharp gradient of suspended particulate matter concentrations (SPM) from >100 g m^{-3} in the near-shore waters to <0.5 g m^{-3} offshore. Tidal

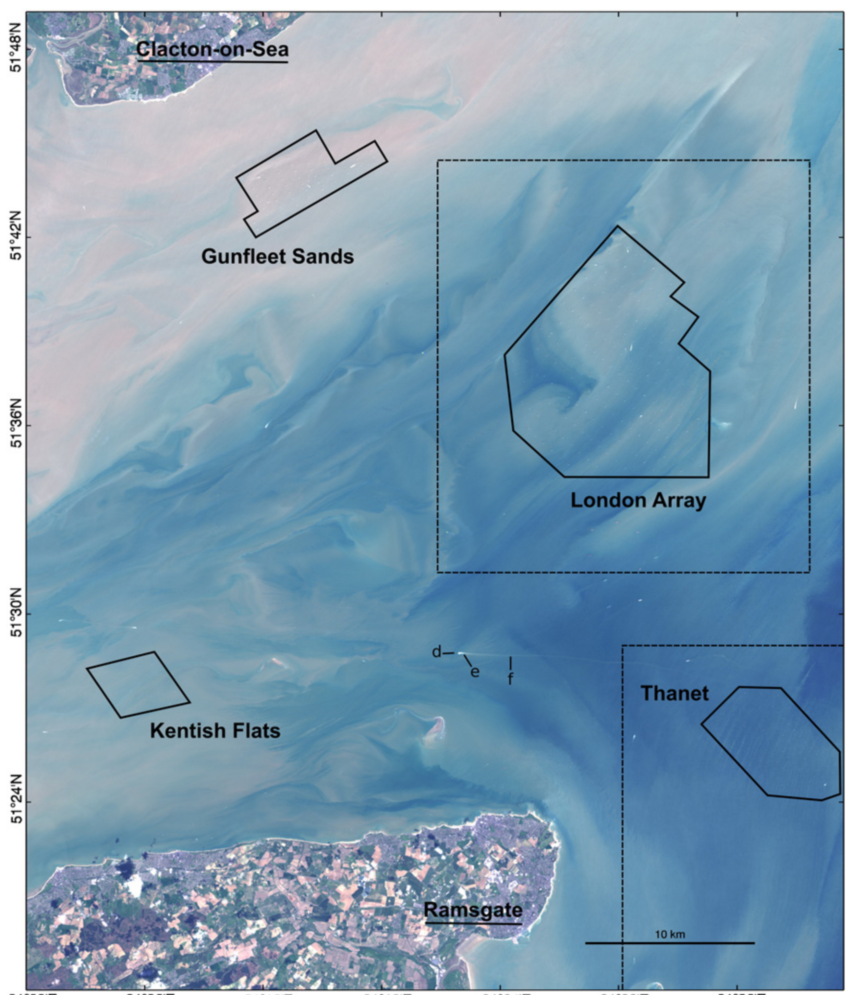

Fig. 1. RGB composite (channels 4-3-2) of a part of the L8/OLI image on 2013-04-28 at 10:54 UTC, showing the suspended sediments (brown-reddish colors) in the Thames estuary. Large ships can be seen as white spots, sometimes with an attached wake. Four wind farms are marked: the London Array, Thanet, Gunfleet Sands and Kentish Flats. Coverage of Figs. 6 and 7 (partially) is shown by the dashed lines. Spectra for points d, e and f are shown in Fig. 5.

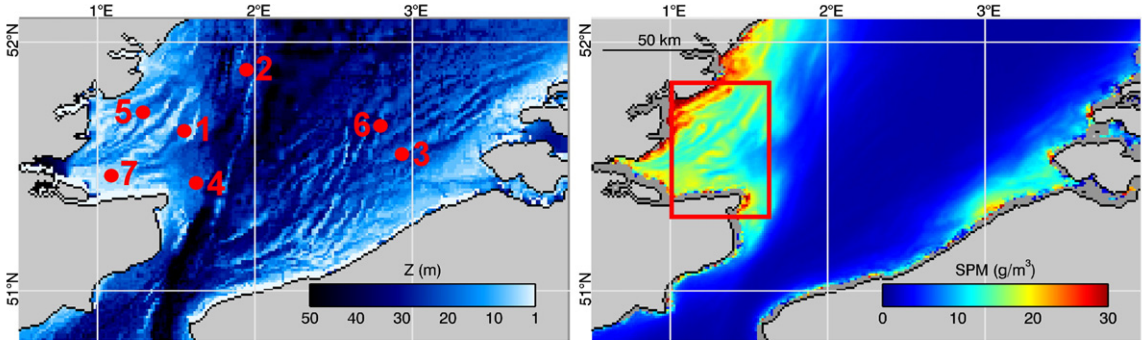

Fig. 2. Left: the bathymetry of the southern North Sea (Smith & Sandwell, 1997, version 14.1). Locations of the wind farms in Table 1 are plotted in order of nameplate capacity. Right: 2003–2012 mean average MODIS-derived suspended particulate matter concentration, SPM (Nechad et al., 2010), processing details in Vanhellemont and Ruddick (2011). The extent of Fig. 1 is plotted on the right figure.

currents are often >1 ms^{-1} (United Kingdom Hydrographic Office, 1985, 1995). SPM patterns observed at the water surface are closely linked to bathymetry (Fig. 2) because of resuspension of seafloor sediments by semidiurnal tides and by winds. In turbid waters SPM dominates the attenuation of light (Devlin et al., 2008) and thus has a major impact on primary production by phytoplankton. For example, even in the eutrophic Colne estuary (N–W corner of Fig. 1), phytoplankton is light limited most of the year because of the high turbidity (Kocum, Underwood, & Nedwell, 2002). Water turbidity greatly impacts the vision of harbor seals (Weiffen, Möller, Mauck, & Dehnhardt, 2006), and pursuit-diving birds (Strod, Arad, Izhaki, & Katzir, 2004). In general, the impact of predation risk for fish is reduced in turbid waters (Abrahams & Kattenfeld, 1997; Maes, Taillieu, Van Damme, Cottenie, & Ollevier, 1998), and turbidity might have a structuring effect on fish communities (Utne-Palm, 2002). SPM mapping is also of interest for underwater visibility estimation for diving observations and for dredging operations (Wu, de Leeuw, Skidmore, Prins, & Liu, 2007), both for real-time operations, and in conjunction with sediment transport models (Fettweis, Nechad, & Van den Eynde, 2007), to understand dredging requirements.

2.2. Satellite data

Landsat 8 (L8) was launched on February 11, 2013 and normal operations started on May 30, 2013. L8 has a ground track repeat cycle of 16 days with an equatorial crossing time at 10:00 a.m. The Operational Land Imager (OLI) on L8 (Table 2) is a nine band push broom scanner with a swath width of 185 km and eight channels at 30 m and one panchromatic channel at 15 m spatial resolution. Compared to the Thematic Mapper (L4-5/TM) and the Enhanced Thematic Mapper Plus (L-7/ETM+) carried on previous Landsat missions, L8/OLI offers higher signal-to-noise ratios (SNR) – mainly because of longer integration times on the push broom scanner – and a better quantization (12 instead of 8 bits for radiometric digitization). In this study, SPM is retrieved using OLI bands 4 (630–680 nm), and 5 (845–885 nm). Two images of the Thames estuary containing five offshore wind farms will be considered in detail (Table 3). Orthorectified and terrain corrected Level 1T OLI imagery was obtained from USGS EarthExplorer (http://earthexplorer.usgs.gov/). Imagery was processed by the Level 1 Product Generation System (LPGS) versions 2.2.2 and 2.2.3 and is provided in GeoTIFF format with UTM projection and WGS84 datum. Tidal information for both images is provided in Table 4.

The atmospheric correction applied in this paper is fully described in Appendix A. Top of atmosphere reflectance in bands 4 and 5, respectively red and near infrared, is derived from the L1T files. Images are corrected for scattering by molecules (Rayleigh) and aerosols to retrieve water-leaving radiance reflectance, ρ_w, in the red band. Aerosol reflectance is estimated using an approach similar to Ruddick, Ovidio, and Rijkeboer (2000), assuming a constant aerosol type over the scene and a constant ratio of water-leaving reflectances in bands 4 and 5.

Two images (listed in Table 3) from the Moderate Resolution Imaging Spectroradiometer (MODIS) on the Aqua satellite (EOS-PM) were used for validation of the Landsat 8 processing presented here. MODIS images were obtained from the NASA Ocean Biology Processing Group (OBPG). The high resolution (250 m) 645 nm band was processed from L1A to L2 in SeaDAS 7.0 using the standard approach (Gordon & Wang, 1994a), extended with the iterative turbid water NIR-modeling method (Bailey, Franz, & Werdell, 2010). The standard BRDF correction that uses the computed chlorophyll *a* concentration was disabled in these turbid waters.

Suspended particulate matter concentration (SPM) is computed from ρ_w using the single band algorithm of (Nechad et al., 2010):

$$SPM = \frac{A\rho_w}{1\text{-}\rho_w/C} \tag{1}$$

where for OLI band 4 the tabulated values for 655 nm are used: A = 289.29 g m^{-3} and C = 0.1686. For MODIS/Aqua, the 645 nm band-specific values are used: A = 258.85 g m^{-3} and C = 0.1641.

Table 2
L8/OLI bands with wavelength, ground sampling distance, GSD, signal-to-noise ratio, SNR; at reference radiance, L.
Irons, Dwyer, & Barsi (2012).

Band	Wavelength (nm)	GSD (m)	SNR at reference L	Reference L (W m^{-2} sr^{-1} μm^{-1})
1 (Coastal/Aerosol)	433–453	30	232	40
2 (Blue)	450–515	30	355	40
3 (Green)	525–600	30	296	30
4 (Red)	630–680	30	222	22
5 (NIR)	845–885	30	199	14
6 (SWIR 1)	1560–1660	30	261	4
7 (SWIR 2)	2100–2300	30	326	1.7
8 (PAN)	500–680	15	146	23
9 (CIRRUS)	1360–1390	30	162	6

Table 3
L8/OLI images of the Thames estuary used in this paper. Corresponding MODIS Aqua 5-minute granules have also been listed.

Image	Date (ISO8601)	Time	Processor	MODIS-Aqua
LC82010242013118LGN01	2013-04-28	10:54 UTC	LGPS 2.2.2	12:05 UTC
LC82010242013246LGN00	2013-09-03	10:54 UTC	LGPS 2.2.3	12:05 UTC

Table 4
Harmonic tide predictions from XTide (http://www.flaterco.com/xtide/) for reference station Dover (51.1144°N, 1.3225°E). Tidal phase at Dover with respect to high water (HW) and time since current reversal (ΔT, at each wind farm) are estimated from the tide predictions and the Admiralty Tidal Stream Atlas (United Kingdom Hydrographic Office, 1985, 1995, 2005).

Date (ISO8601)	High tide (UTC)	Low tide (UTC)	Tidal phase (Dover)	Range	Wind farm	ΔT
2013-04-28	00:27/12:50	07:41/20:03	HW − 2 h	0.0–7.3 m	London Array	4–5 h
					Thanet	5–6 h
2013-09-03	09:53/22:13	04:29/16:50	HW + 1 h	1.6–6.1 m	London Array	0–1 h
					Thanet	1–2 h

3. Results

3.1. Comparison with MODIS/Aqua

A qualitative comparison of MODIS and OLI scenes shows that both sensors reveal similar patterns of SPM (Fig. 3). The much higher resolution of OLI – about 8 × 8 pixels to the MODIS pixel – is immediately apparent. The absolute SPM values are also comparable: both sensors retrieve SPM between 5 and 30 g m^{-3}. Also here the resolution difference can be observed: a large range of OLI SPM values is found for a single MODIS pixel. After spatially averaging the OLI pixels, the range of OLI values in the comparison with MODIS is reduced. The high SNR ratio of OLI leads us to believe that the imager is capable of retrieving the spatial variability at its native scale (see Section 3.2). The coherent spatial

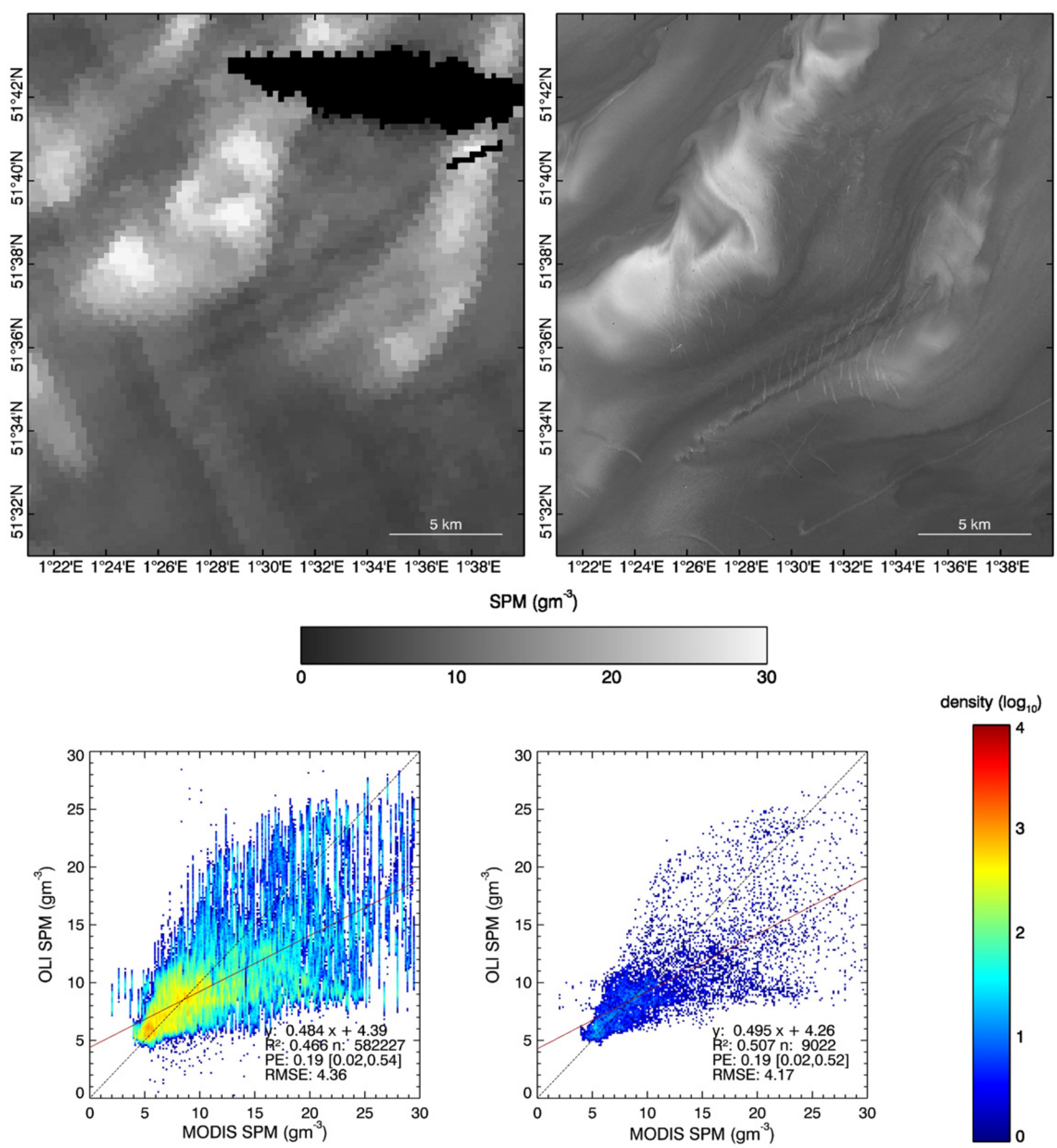

Fig. 3. Top row: MODIS Aqua (left) and L8/OLI (right) suspended particulate matter maps for the London Array, on 2013-09-03 (a larger version of the OLI image is shown in Fig. 6b). The black patch in the MODIS data is missing data due to cloud flagging. The lower plots show the comparison of OLI against MODIS data, left at ~OLI resolution and right at ~MODIS resolution. The colors denote pixel densities in log scale. The dashed line is the 1:1 line, the solid red line is the ordinary least squares regression line.

structures in the OLI image also indicate that the vertical striping in the scatterplot is actual spatial variability rather than noise. When the OLI data is spatially averaged to several coarser grids, it is found that this striping is very noticeable when the loss of spatial detail becomes significant (see Section 3.4). The full OLI-MODIS comparison for both wind farms and both images is given in Supplementary Data 1.

3.2. Noise equivalent SPM (SNR requirements)

The signal to noise ratio (SNR) determines whether a sensor can be used for a given application, or what level of spatial or temporal averaging is required to reach the desired performance. To compare the performance of different sensors, the noise-equivalent reflectance, NE_ρ, or the expected uncertainty on reflectance due to sensor noise, is computed:

$$NE_\rho = \frac{\pi \cdot NE_L \cdot d^2}{F\theta \cdot \cos\ \theta_s} \tag{2}$$

where $F0$ is the extraterrestrial solar irradiance and $\theta 0$ the sun zenith angle. The earth–sun distance in Astronomical Units, d, varies ~3.5% over the year, but is here set to 1 AU as the variability of NE_ρ due to changes in θ_s is much larger (Eq. 2). NE_L is the noise-equivalent radiance:

$$NE_L = \frac{L_{ref}}{SNR} \tag{3}$$

with SNR the signal-to-noise ratio at the reference radiance, L_{ref}. SNR and L_{ref} values for several (red) bands on different sensors are given in Table 5. The noise-equivalent SPM (NE_{SPM}) can be estimated from NE_ρ using the linear approximation of Eq. (1) (the numerator). Fig. 4 shows NE_{SPM} for the bands listed in Table 5 as function of $\theta 0$. Most of these bands are designed for land and cloud applications and have a relatively high NE_{SPM}, clearly increasing with $\theta 0$. The only dedicated ocean color band considered here (MODIS 13) has a very high SNR and a correspondingly low NE_{SPM}. At native resolution, OLI 4 and MODIS 1 show a similar performance of NE_{SPM} ~0.1 g m^{-3} for $\theta_s < 50°$, increasing rapidly to >0.3 g m^{-3} for larger $\theta 0$. MODIS1 is a high resolution (250 m) land band and is typically aggregated to 1 km for ocean color processing, which will reduce noise by a factor of 4. For the OLI images in Table 3, $\theta 0$ were 36° and 40°, giving an estimated NE_{SPM} of <0.1 g m^{-3}. The L7/ETM + band is especially noisy, and a spatial binning to 9 × 9 pixels (270 m) is required to reach the NE_{SPM} level of OLI. Actually further binning to 11 × 11 pixels (330 m) is required, as the limited digitization (8 bits) of the ETM + introduces additional noise to the order of ~74% of the NE_{SPM}. SEVIRI has a high temporal frequency (15 min, 5 min in rapid scan mode) and the noise can be reduced by temporal averaging. For example, in Vanhellemont, Neukermans and Ruddick (2013) a 5-image averaging was used that retained temporal variability, and reduced the NE_{SPM} given in their Fig. 4 by $\sqrt{5}$.

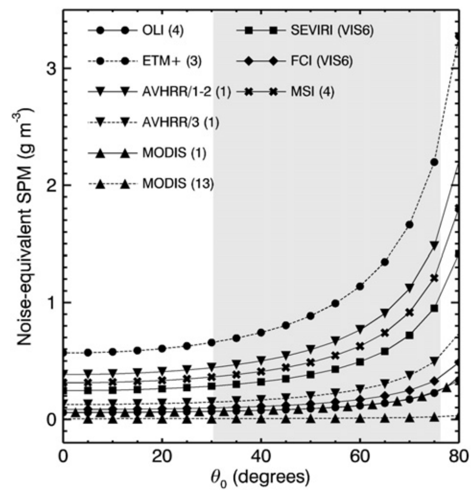

Fig. 4. Noise-equivalent SPM as a function of $\theta 0$, calculated using the SNR values in Table 5. The shaded area represents the annual range of $\theta 0$ at 52°N, 2°E at 11 UTC.

3.3. Top of atmosphere spectral shape

The brown color of the turbine monopile wakes on the RGB composites gives a strong qualitative indication that they are sediment plumes rather than atmospheric effects or foam/white caps. This is investigated quantitatively here. In Fig. 5, ρ_{TOA} (reflectance at Top Of Atmosphere) spectra are shown for points inside and just outside the turbine monopile wakes a–b) as well as a contrasting example from a boat c) and its wake d–e). The inside and outside points are close together (~100 m) so it can be assumed that from the sensor's perspective the atmosphere is identical. Thus, the difference in ρ_{TOA} (inside–outside) removes the atmospheric signal and represents the signal from the extra optically active constituents in the wake. The turbine monopile wake pixels a) and b) show a typical turbid water spectrum (e.g. Fig. 5 in Doxaran et al., 2002 and Fig. 7 in Ruddick, De Cauwer, Park, & Moore, 2006) with a strong reflectance in the red band (B4). This increase of ~0.01 sr^{-1} corresponds to a ΔSPM of ~3 g m^{-3}, i.e. a difference with the ambient SPM larger than the estimated NE_{SPM} (see paragraph 3.2). The boat pixel shows a much larger, and spectrally flat, increase in reflectance. The boat's wake just after the stern also shows a flat and rather large increase in reflectance (note the scale difference with the turbine wakes), probably caused by foam on the sea

Table 5
Red bands on several sensors with extraterrestrial solar irradiance, F0, signal-to-noise ratio, SNR, at reference radiance, L_{ref}. L_{ref} for AVHRR and FCI were computed using reference reflectance, ρ_{ref}, of 0.05 sr^{-1} and 0.1 sr^{-1} respectively.

Sensor	Wavelength (band)	F0 (W m^{-2} µm^{-1})	SNR at L_{ref}	L_{ref} (W m^{-2} sr^{-1} µm^{-1})	Reference
L8/OLI	655 nm (4)	1549	222	22	Irons et al. (2012)
L7/ETM+	660 nm (3)	1533	26	22	Irons et al. (2012)
AVHRR/1-2	630 nm (1)	1643[a]	3	2.61	Kidwell (1998)
AVHRR/3	630 nm (1)	1643[a]	9	2.61	Kramer (2002)
Aqua/MODIS	645 nm (1)	1578	140	16.5	Franz et al. (2006)
Aqua/MODIS	667 nm (13)	1523	1962	14.7	Franz et al. (2006)
MSG-1/SEVIRI	635 nm (VIS6)	1618	10.1	5.33	Govaerts and Clerici (2004)
MTG-1/FCI	645 nm (VIS6)	1589[a]	30	5.06	MTG Mission Requirement Document (2007)
Sentinel-2/MSI	665 nm (4)	1536[a]	7.7 (at L_{min})	3.31 (L_{min})	Drusch, Gascon, and Berger (2010)

[a] Band center F0 (Thuillier et al., 2003).

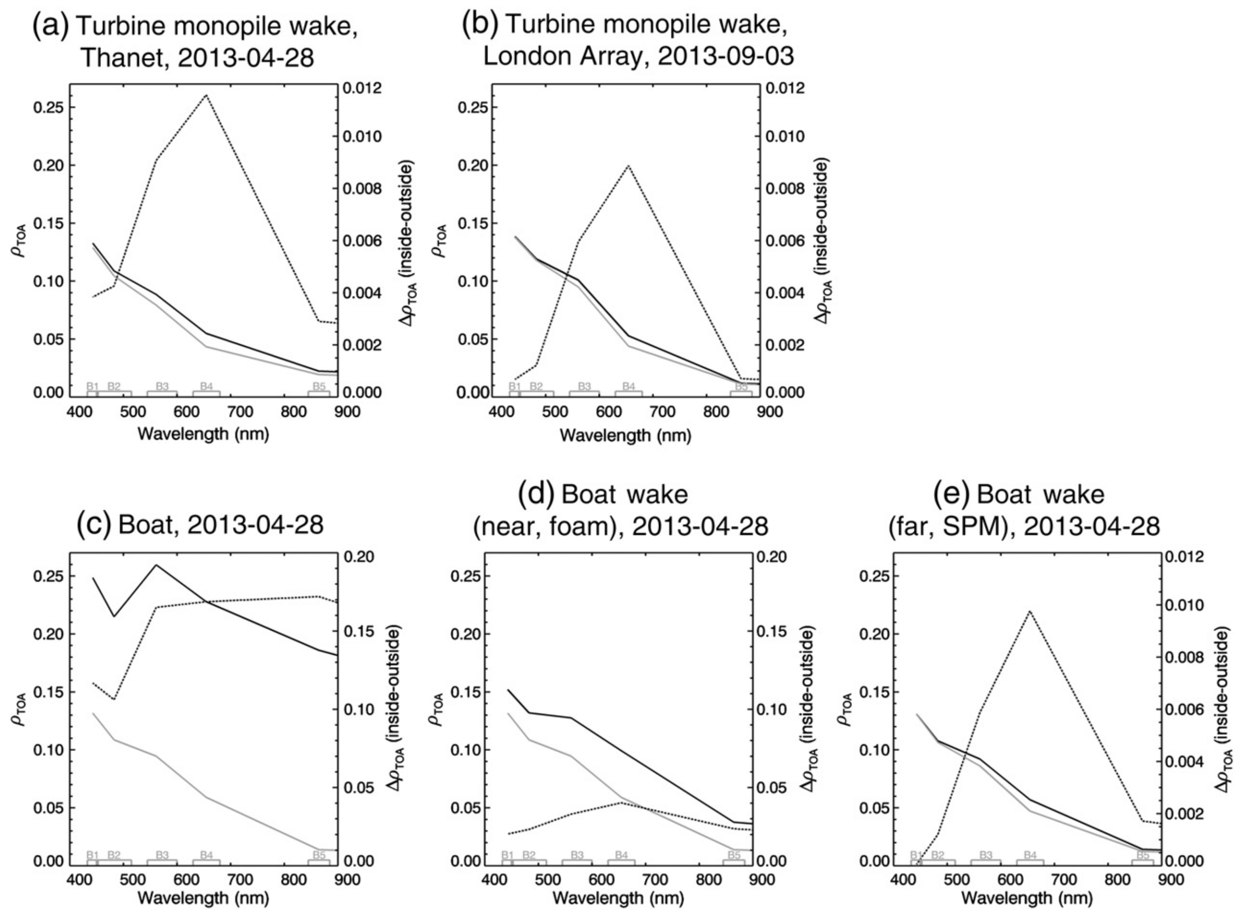

Fig. 5. Spectra for five targets: two turbine monopile wakes, a) Thanet 2013-04-28 (see Fig. 7a), and b) London Array, 2013-09-03 (see Fig. 6b), and c) a boat, its wake d) just behind the stern and e) several km from the stern (2013-04-28, see Fig. 1). The top of atmosphere reflectance (ρ_{TOA}) spectra are drawn in black and gray for points just inside and outside the target (left axis). The difference between the two is plotted in the dashed black line (right axis). Note the brightness difference between the turbid wakes (a,b and e) and the boat and foam (c and d). A different scaling of the right axis was used for the latter two. OLI band widths are plotted on the x axis.

surface. Further away from the stern (in this case ~2 km) the boat wake is brown, with a large reflectance in the red band, showing the temporary effect of large vessels on SPM in shallow waters.

3.4. Wind turbine wakes

Suspended particulate matter concentration (SPM) maps for both wind farms on both images are given in Figs. 6 and 7. High SPM is found to be associated with shallow sand banks, and small scale eddies are observed on fronts between clear and turbid waters. Turbid ship wakes of several kilometers in length are visible. A striking observation is that sediment plumes are associated with the wakes of individual turbine monopiles of offshore wind farms. From Fig. 5 it is clear that the brown color of these wakes is caused by an in-water wake phenomenon (SPM) and not an atmospheric wake or air–sea interface phenomenon. The observed plume width is between 1 and 5 pixels, or 30–150 m. The wakes are aligned with the tidal streams (arrows in Figs. 6 and 7). The length of these sediment plumes is one to several km, and is longer for the 2013-04-28 image, presumably because of the longer time since current reversal. On Fig. 7a, the wakes in the farm show a regular pattern around the turbines extending far downstream. In the deeper gulley just south of the farm, the ambient SPM concentration is lower. The regularly spaced pattern appears again on the shallow sand bank, more than 10 km downstream. This length scale correlates well with the average current velocity and the time since current reversal (~5 h, Table 4). The more recent current reversal in Fig. 7b is also clear from the irregular shape of the plumes.

3.5. Impact of spatial resolution demonstrated by degrading OLI/L8

To assess the value of high resolution imagery for coastal water monitoring, OLI SPM data was spatially averaged to several coarser grids. Fig. 8 shows the OLI data for the London Array on 2013-09-03, spatially averaged to 150, 300 and 900 m grids. A comparison of the native resolution (30 m) and resampled data is shown in the scatter plots. The vertical striping in the density plots shows the variability observed within one aggregated pixel. This variability corresponds to the small scale features such as boat and monopile wakes, small eddies and fronts. The turbid wakes of ships and wind turbines are still visible in the 150 m data depending on the image and location, i.e. when the contrast with the surrounding waters is high. Spatial detail is quickly lost at coarser resolutions, which is also manifested by the increased vertical striping in the scatterplot. While the increased turbidity could be measured in the moderate resolution pixel, it would be difficult to detect, as it will be (much) smaller than the short term SPM changes in the region (see e.g. Figs. 5 through 7 in Vanhellemont, Neukermans et al., 2013). The spatial information will be absent, as many features are smaller than the moderate pixel resolution. From the images we present (Figs. 6 and 7) it is clear that the spatial resolution can be an essential factor in understanding changes in surface SPM. At 300 m the larger scale coastal and estuarine features associated with sand banks are

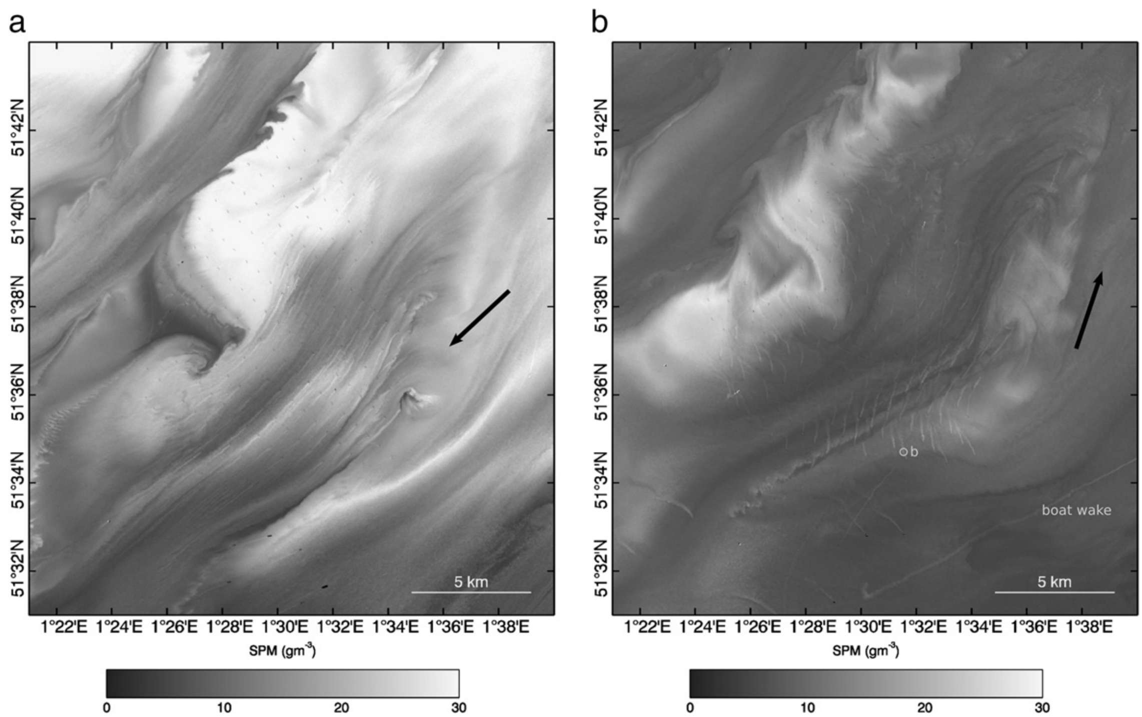

Fig. 6. L8/OLI SPM maps. Missing or masked data is plotted in black. The arrows represent the direction of the tidal current according to the tidal phase at the time of the image (Table 4), derived from the tidal stream atlas (UKHO, 1995). a) the London Array on 2013-04-28 (10:54 UTC). Individual turbine monopiles can be distinguished as dots, especially in the higher SPM areas. The objects masked in black in the south of the image are ships that are bright and spectrally white (e.g. Fig. 5), also with attached turbid wakes.b) the London Array on 2013-09-03 (10:54 UTC). Spectra for point b are shown in Fig. 5.

much better represented than at 900 m. The value of imagery at this spatial resolution, similar to the MERIS full resolution mode and the MODIS high resolution bands, for coastal zone research is clear. The full set of resampled data is shown in Supplementary Data 2.

4. Discussion

A significant increase in suspended sediments has been observed in the wakes of individual turbine monopiles in offshore wind farms. The

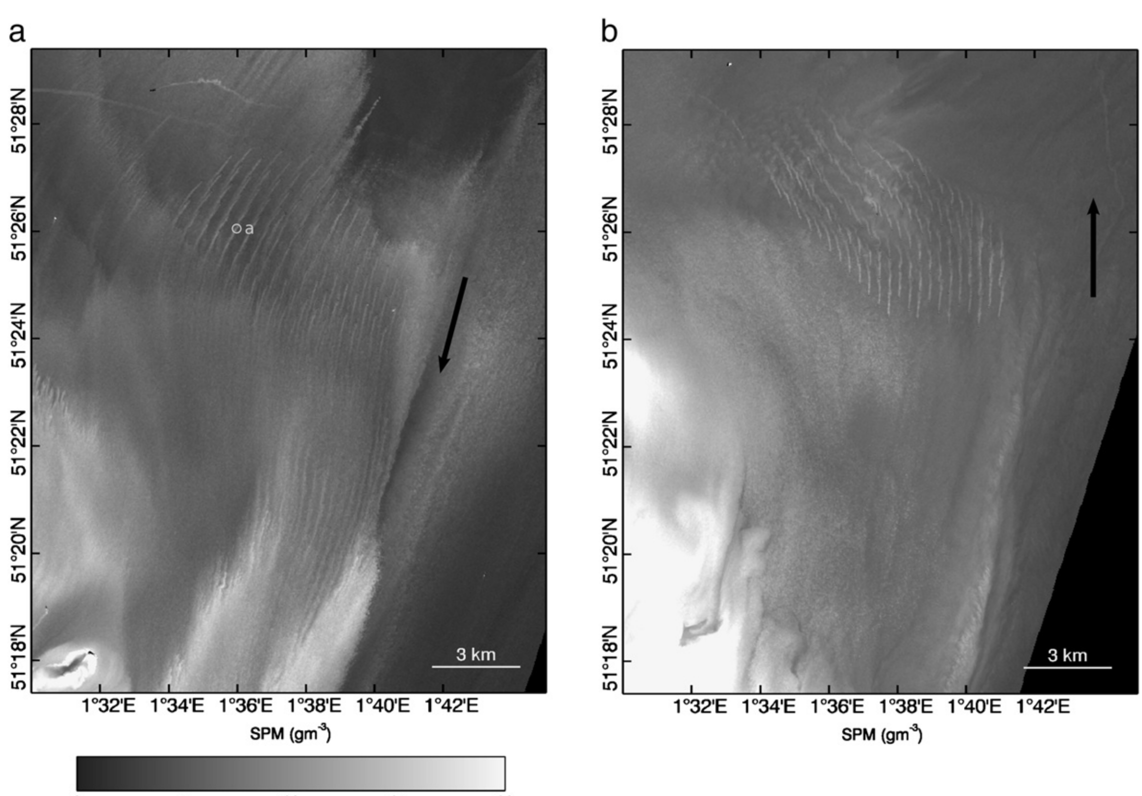

Fig. 7. Same as Fig. 6 a) the Thanet wind farm on 2013-04-28 (10:54 UTC). Spectra for point a are shown in Fig. 5. b) the Thanet wind farm on 2013-09-03 (10:54 UTC).

wakes are aligned with the tidal streams and their direction changes with the tide. The plumes are 30–150 m wide and typically extend 1 or more km downstream from the turbine. The extent of the plumes of the Thanet farm on 2013-04-28 seems to exceed 10 km. The plume length is likely related to the time-integrated current since reversal and particle settling velocity. SPM concentration could depend on seafloor sediment type and water depth as well as artificial seafloor modifications (scour protection etc.).

Impacts of these turbid turbine wakes are currently unknown, but the spatial extent is considerable and the turbidity change may be persistent (repeating each current reversal), warranting further research on their environmental impact. Changes in the underwater light field affect for example primary production and visual predation. The observed wakes suggest changes in sedimentation patterns that could potentially cause bathymetric modification. The source of the suspended sediment is unclear, and has to be investigated: if the material is eroded at the base of the turbine, additional scour protection might be required. Scour pits can form quickly around monopile structures, they are aligned with the current and can be partially filled in after tide reversal (Whitehouse, Harris, Sutherland, & Rees, 2011). Scour depths depend on pile diameter, currents, waves, water depth and seafloor sediment (Whitehouse et al., 2011). At the wind farms discussed here, scour protection is currently only installed for cable crossings and offshore substations at the London Array, and for certain sections of the export cable at Thanet.

The results from our simple OLI processing compare well to the established MODIS-Aqua data, and we are confident in the retrieved patterns of SPM. Even the absolute retrievals are in good agreement,

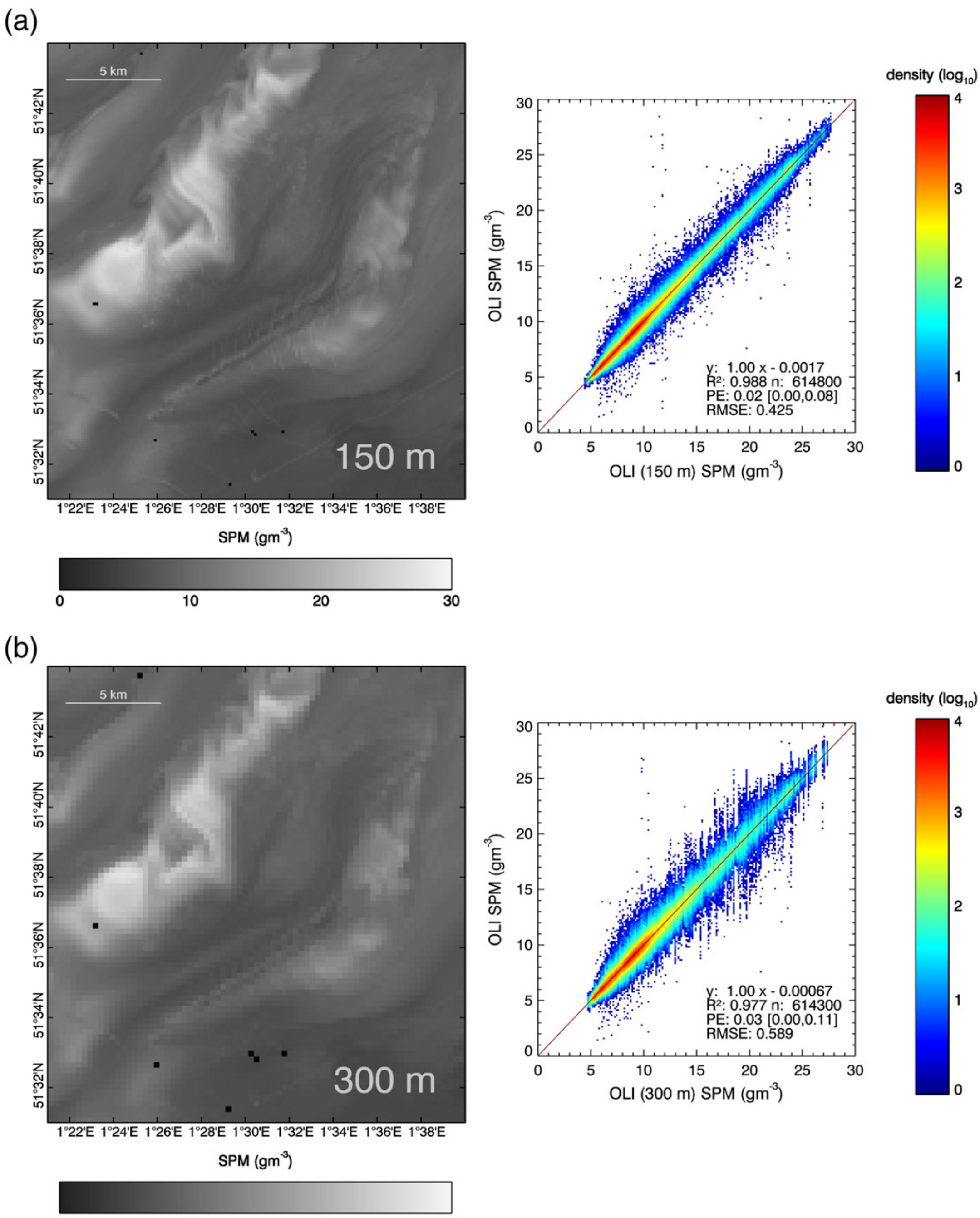

Fig. 8. OLI data for the London Array on 2013-09-03 (see Fig. 6b) averaged to 150, 300 and 900 m (top to bottom rows), and scatterplots of OLI data at native resolution (30 m) as function of the resampled data. The colors in the scatter plots denote pixel densities in log scale.

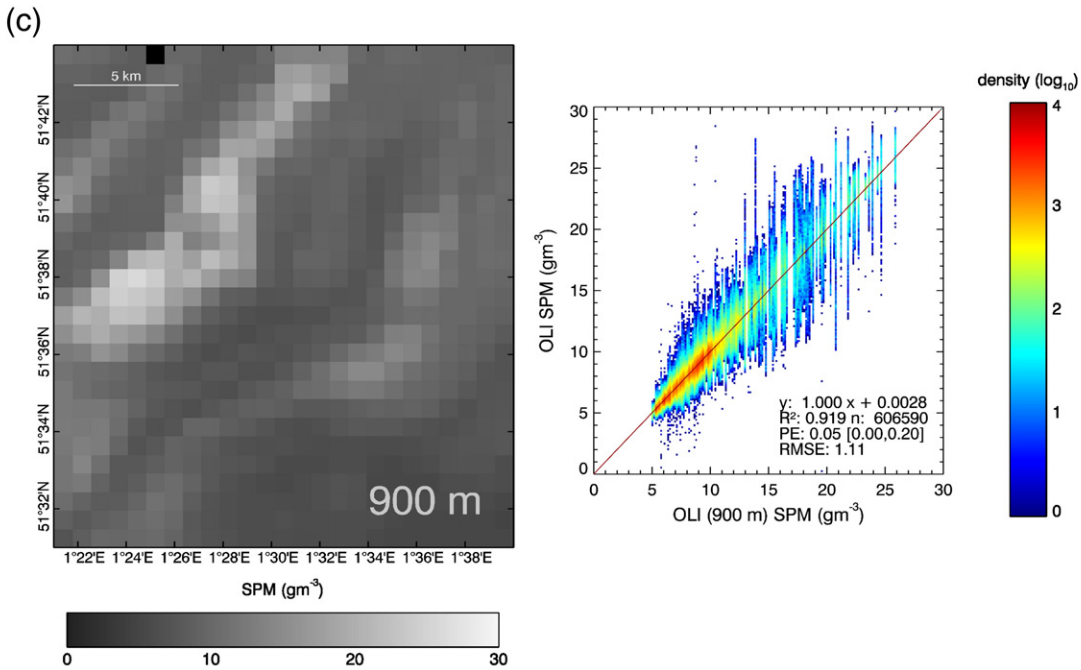

Fig. 8 (*continued*).

especially considering the temporal dynamics of the region and the large differences in viewing conditions and sensor design. In both MODIS scenes, the view zenith angle for the study area is quite large, ~50°, therefore the geometric distortion in the images is large as well, causing a spatial mismatch with the nadir-viewed OLI data. This spatial mismatch introduces rather large errors especially due to the resolution difference of the sensors (OLI: 30 m, MODIS: 250 m). Moreover, due to the scanning system of MODIS, these edge of swath pixels have a much larger footprint than the central ~250 m pixels, with significant overlap between scan lines (the so called 'bow-tie effect'). The bidirectionality of the marine reflectance in turbid waters is not accounted for in the processing and there is a considerable difference in viewing geometry between these OLI and MODIS images. Furthermore, there is a one hour difference between their acquisition, which in this region can already cause significant differences in surface SPM concentrations (Vanhellemont, Greenwood et al., 2013; Vanhellemont, Neukermans et al., 2013). For example, considerable discrepancies have also been found when two images from adjacent swaths of MODIS-Aqua, with different viewing angles and spaced ~100 min apart, are compared (e.g. Fig. 9 in Vanhellemont, Neukermans et al., 2013). As such differences exist within the same system, we have not attempted to assess the differences caused by the different atmospheric correction approaches used for MODIS (SeaDAS) and OLI (this paper). Uncertainties on the OLI calibration could cause significant systematic discrepancies in the comparison, but it is too early in the Landsat 8 mission to have a good estimate of calibration performance.

With these results from L8/OLI, the advantages of high resolution imagery for offshore applications are clear. The high spatial resolution (30 m) resolves small scale turbidity features, and the high patchiness of the suspended sediments in coastal waters can be studied. By spatially averaging OLI data (Fig. 8) it is illustrated that observation of the impact of the turbine wakes on turbidity is impossible with moderate resolution satellite data such as MODIS/Aqua. Next to L8/OLI, other high resolution and very high resolution sensors could be used to monitor the turbid wakes from offshore turbines. For quantitative monitoring of suspended sediment concentrations, sensors are needed with a red and near infrared band for aerosol correction, sufficiently high signal:noise ratio (see e.g. Section 3.2) and good digitization (10 or 12 bit). For example, the RapidEye System has a multispectral push broom scanner with a 6.5 m ground resolution and suitable bands (630–685 and 760–850 nm). Pléiades has a 2 m resolution multispectral imager with similar but wider bands (600–720 and 750–950 nm). These programs have constellations of identical satellites (currently: 5 RapidEye and 2 Pléiades) that can provide improved temporal coverage. Older Landsat data (TM/ETM+) have similar bands to L8/OLI, but radiances are digitized using only 8 bit and for marine application the images are quite noisy at native resolution. Many other missions with suitable bands that could be investigated are currently flying, such as SPOT, IKONOS, Quickbird, Worldview-1, and Worldview-2. A future mission of interest is Sentinel-2, with expected launch in 2014. Sentinel-2 will routinely cover coastal regions with 13 bands at 10–60 m spatial resolution, including 10 m red and near infrared bands with central wavelengths 665 and 842 nm.

Supplementary data to this article can be found online at http://dx.doi.org/10.1016/j.rse.2014.01.009.

Acknowledgments

NASA is thanked for the MODIS/Aqua data and the SeaDAS processing software. USGS is thanked for the distribution of OLI/Landsat 8 data. Rodney Forster is thanked for the idea of using Landsat 8 for monitoring wind farms and their impact on suspended sediments. The image processing software used here was developed in the framework of the JELLYFOR project, funded by the Belgian Science Policy Office STEREO program (contract SR/37/135).

Appendix A. Atmospheric correction of OLI imagery

The simple atmospheric correction for the Operational Land Imager (OLI) on board of Landsat 8 (L8) is described in this appendix. Band averaged values of solar irradiance, F0 (Thuillier et al., 2003), water absorption, a_w (Kou, Labrie, & Chylek, 1993; Pope & Fry, 1997), Rayleigh optical thickness, τ_r (Bodhaine, Wood, Dutton, & Slusser, 1999), and Ozone optical thickness, τ_{oz} (Anderson, Hupalo, & Mauersberger, 1993, 1990; Anderson, Maeder, & Mauersberger, 1991; Anderson & Mauersberger, 1992; Anderson, Morton, & Mauersberger, 1990;

Burkholder & Talukdar, 1994) were calculated by convoluting the OLI relative spectral response function (Barsi, Markham, & Pedelty, 2011) over values tabulated by Bryan Franz (http://oceancolor.gsfc.nasa.gov/DOCS/RSR_tables.html).

Table A1
L8/OLI bands with band averaged extraterrestrial solar irradiance, F0, pure-water absorption, a_w, Rayleigh optical thickness for a standard atmosphere, τ_R and ozone optical thickness for 300 DU of atmospheric ozone; τ_{oz}.

Band	F0 ($W\ m^{-2}\ \mu m^{-1}$)	a_w (m^{-1})	τ_R (unitless)	τ_{oz} (unitless)
1 (Coastal/Aerosol)	1895.6	$7.24 \cdot 10^{-3}$	$2.35 \cdot 10^{-1}$	$8.79 \cdot 10^{-4}$
2 (Blue)	2004.6	$1.56 \cdot 10^{-2}$	$1.69 \cdot 10^{-1}$	$5.87 \cdot 10^{-3}$
3 (Green)	1820.7	$6.96 \cdot 10^{-2}$	$9.02 \cdot 10^{-2}$	$3.14 \cdot 10^{-2}$
4 (Red)	1549.4	$3.74 \cdot 10^{-1}$	$4.79 \cdot 10^{-2}$	$1.82 \cdot 10^{-2}$
5 (NIR)	951.2	$4.63 \cdot 10^{1}$	$1.55 \cdot 10^{-2}$	$6.43 \cdot 10^{-4}$
6 (SWIR 1)	247.6	$7.76 \cdot 10^{2}$	$1.28 \cdot 10^{-3}$	0
7 (SWIR 2)	85.5	$2.26 \cdot 10^{3}$	$3.70 \cdot 10^{-4}$	0
8 (PAN)	1724.0	$1.80 \cdot 10^{-1}$	$7.94 \cdot 10^{-2}$	$2.66 \cdot 10^{-2}$
9 (CIRRUS)	367.0	$5.09 \cdot 10^{2}$	$2.40 \cdot 10^{-3}$	0

A.1. Top of atmosphere reflectance

Top of atmosphere (TOA) radiances, L_{TOA}, were computed from Digital Numbers (DN) in bands 4 and 5:

$$L_{TOA} = M_L \cdot DN + A_L \tag{A1}$$

with M_L (multiplicative factor, gain) and A_L (additive factor, offset) values provided in the LPGS metadata file. TOA reflectances (ρ_{TOA}) were computed by normalizing L_{TOA} to the band averaged solar irradiance:

$$\rho_{TOA} = \frac{\pi \cdot L_{TOA} \cdot d^2}{F0 \cdot \cos\theta_0} \tag{A2}$$

where d is the earth–sun distance in Astronomical Units, θ_0 the sun zenith angle and $F0$ the band averaged solar irradiance. ρ_{TOA} represents the sum of reflectances observed by the sensor:

$$\rho_{TOA} = \rho_r + \rho_a + \rho_{ra} + \rho_g + t_0 t_v (\rho_w + \rho_{wc}) \tag{A3}$$

where ρ_r and ρ_a, are the reflectances resulting from Rayleigh and aerosol scattering. ρ_{ra} represents the interaction between the two and can be included in the multiple scattering ρ_a estimation. ρ_g is the specular reflection of the sun which will be ignored as in the study area the sun zenith angle (θ_0) is always much larger than the viewing zenith angle (θ_v). t_0 and t_v are the sun–sea and sea-sensor diffuse transmittances. ρ_{wc} is the reflectance of foam and whitecaps and can be estimated from wind speed using an empirical relationship. Here we ignore ρ_{wc}, and it is assumed to be largely corrected for in the aerosol correction (Gordon & Wang, 1994b). ρ_w is the parameter of interest, marine reflectance, or water-leaving radiance reflectance, defined as π times the water-leaving radiance divided by above-water downwelling irradiance. For the atmospheric correction in this paper we simplify ρ_{TOA} to:

$$\rho_{TOA} = \rho_r + \rho_a + t_0 t_v \rho_w. \tag{A4}$$

For each band the diffuse transmittance for the sun–sea (t_0) and sea-sensor (t_v) paths are estimated by substituting θ by θ_0 and θ_v in:

$$t = \exp\left[-\left(\frac{\tau_r}{2} + \tau_{oz}\right)/cos\theta\right] \tag{A5}$$

where τ_r and τ_{oz} are the band averaged Rayleigh and Ozone optical thicknesses for a standard atmosphere (see Table A1). Water vapor absorption and aerosol impact on atmospheric transmittance are currently ignored in the processing, adding a few percent uncertainty on the final OLI product, but not affecting the spatial features.

A.2. Rayleigh correction

The Rayleigh reflectance, ρ_r, is estimated (Gordon, Brown, & Evans, 1988) according to:

$$\rho_r = \tau_r \cdot p_r(\theta_0, \theta_v, \Delta\phi) \cdot (4\cos\theta_0 \cos\theta_v)^{-1} \tag{A6}$$

where $\Delta\phi$ is the relative azimuth angle between sun and sensor, and with

$$p_r(\theta_0, \theta_v, \Delta\phi) = P_r(\theta_-) + [r(\theta_v) + r(\theta_0)] \cdot P_r(\theta_+) \tag{A7}$$

where the scattering angles $\theta_\pm$ represent the Rayleigh contribution from photons that have not interacted with the sea surface (θ_-) and from photons that have been specularly reflected by the sea surface before or after scattering (θ_+). θ_- and θ_+ are calculated from sun-sensor geometry:

$$\cos\theta_\pm = \pm\cos\theta_0 \cos\theta_v - \sin\theta_0 \sin\theta_v \cos|\phi_0 - \phi_v| \tag{A8}$$

with ϕ_0 and ϕ_v the sun and sensor azimuth angles, and $P_r(\Theta)$ the Rayleigh scattering phase function for scattering angle Θ and $r(\theta)$ the Fresnel reflectance for air-incident rays at an incidence angle θ:

$$P_r(\Theta) = 0.75 \cdot \left(1 + \cos^2\Theta\right) \tag{A9}$$

$$r(\theta) = 0.5 \cdot \left\{\frac{\sin^2(\theta - \theta_t)}{\sin^2(\theta + \theta_t)} + \frac{\tan^2(\theta - \theta_t)}{\tan^2(\theta + \theta_t)}\right\} \tag{A10}$$

$$\theta_t = \sin^{-1}(n_w \sin\theta) \tag{A11}$$

where θ_t is the angle of transmittance and n_w the refractive index of water with respect to air, taken as 1.34. Rayleigh-corrected reflectance (ρ_c) is then obtained after subtraction of ρ_r from ρ_{TOA}:

$$\rho_c = \rho_{TOA} - \rho_r = \rho_a + t_0 t_v \rho_w. \tag{A12}$$

A.3. Aerosol correction

Two further assumptions for the aerosol correction are made, similar to the assumptions in Ruddick et al. (2000) and Neukermans et al. (2009): α, the ratio of marine reflectances in the two bands is constant, here estimated using the average similarity spectrum from (Ruddick et al., 2006) for the band central wavelengths:

$$\alpha = \frac{\rho_w^{(4)}}{\rho_w^{(5)}} = \frac{\overline{\rho}_{wn780}^{(655\,nm)}}{\overline{\rho}_{wn780}^{(865\,nm)}} = \frac{4.734}{0.544} = 8.702 \tag{A13}$$

ε, the ratio of multiple-scattering aerosol reflectances, is constant over the scene:

$$\varepsilon = \frac{\rho_a^{(4)}}{\rho_a^{(5)}}. \tag{A14}$$

In the two OLI bands used here, the constant α derived from a_w is only valid for moderate turbidities, as the relationship will be non-linear at higher marine reflectances (see Fig. 4 of Ruddick et al., 2006). In the images presented in this paper, Eq. (A13) seems to be a good approximation. The aerosol reflectance ratio ε can be derived from clear-water pixels where the water reflectance is negligible and thus where only the aerosols contribute to the TOA signal. On a scatter plot of $\rho_c^{(4)}$

as function of $\rho_c^{(5)}$ these pixels are on a straight line with slope ε. From these scatter plots of the April and September images, ε was respectively set to 0.93 and 0.90. These are unusual values for ε, potentially caused by a calibration bias. After processing with a more standard $\varepsilon = 1$, a decrease in SPM by 2–6% is found for SPM > 5 g m^{-3}, without changing the spatial patterns in the image.

Using the reasoning described by Ruddick et al. (2000), marine reflectance in band 4, $\rho_w^{(4)}$, can be calculated from $\rho_c^{(4)}$ and $\rho_c^{(5)}$:

$$\rho_w^{(4)} = \frac{\alpha}{t_0^{(5)} t_v^{(5)}} \left[\frac{\rho_c^{(4)} - \rho_c^{(5)}}{\alpha\gamma - \varepsilon} \right] \tag{A15}$$

where γ is the ratio of diffuse atmospheric transmittances in the two bands:

$$\gamma = \frac{t_0^{(4)} t_v^{(4)}}{t_0^{(5)} t_v^{(5)}}. \tag{A16}$$

References

Abrahams, M. V., & Kattenfeld, M. G. (1997). The role of turbidity as a constraint on predator–prey interactions in aquatic environments. *Behavioral Ecology and Sociobiology*, *40*, 169–174.

Amos, C., & Alföldi, T. (1979). The determination of suspended sediment concentration in a macrotidal system using Landsat data. *Journal of Sedimentary Research*, *49*, 159–173.

Anderson, S. M., Hupalo, P., & Mauersberger, K. (1993). Ozone absorption cross section measurements in the Wulf bands. *Geophysical Research Letters*, *20*, 1579–1582.

Anderson, S. M., Maeder, J., & Mauersberger, K. (1991). Effect of isotopic substitution on the visible absorption spectrum of ozone. *Journal of Chemical Physics*, *94*, 6351–6357.

Anderson, S. M., & Mauersberger, K. (1992). Laser measurements of ozone absorption cross sections in the Chappuis band. *Geophysical Research Letters*, *19*, 933–936.

Anderson, S., Morton, J., & Mauersberger, K. (1990). Near-infrared absorption spectra of $^{16}O_3$ and $^{18}O_3$: Adiabatic energy of the $^1A_2$ state? *Journal of Chemical Physics*, *93*, 3826.

Bailey, S. W., Franz, B.A., & Werdell, P. J. (2010). Estimation of near-infrared water-leaving reflectance for satellite ocean color data processing. *Optics Express*, *18*, 7521–7527.

Barsi, J. A., Markham, B.L., & Pedelty, J. A. (2011). The operational land imager: Spectral response and spectral uniformity. *SPIE optical engineering + applications* (81530G-81530G).

Bodhaine, B.A., Wood, N.B., Dutton, E. G., & Slusser, J. R. (1999). On Rayleigh optical depth calculations. *Journal of Atmospheric and Oceanic Technology*, *16*, 1854–1861.

Burkholder, J. B., & Talukdar, R. K. (1994). Temperature dependence of the ozone absorption spectrum over the wavelength range 410 to 760 nm. *Geophysical Research Letters*, *21*, 581–584.

Devlin, M., Barry, J., Mills, D., Gowen, R., Foden, J., Sivyer, D., et al. (2008). Relationships between suspended particulate material, light attenuation and Secchi depth in UK marine waters. *Estuarine, Coastal and Shelf Science*, *79*, 429–439.

Doxaran, D., Froidefond, J. -M., Lavender, S., & Castaing, P. (2002). Spectral signature of highly turbid waters: Application with SPOT data to quantify suspended particulate matter concentrations. *Remote Sensing of Environment*, *81*, 149–161.

Drusch, M., Gascon, F., & Berger, M. (2010). *GMES Sentinel-2 mission requirements document*. ESA EOP-SM1163MR-Dr2, 42.

EWEA (2011). Wind in our sails. *Technical report*. European Wind Energy Association.

EWEA (2013). *The European offshore wind industry—Key Trends and Statistics 2012*. European Wind Energy Association.

Fettweis, M., Nechad, B., & Van den Eynde, D. (2007). An estimate of the suspended particulate matter (SPM) transport in the southern North Sea using SeaWiFS images, in situ measurements and numerical model results. *Continental Shelf Research*, *27*, 1568–1583.

Franz, B.A., Werdell, P. J., Meister, G., Kwiatkowska, E. J., Bailey, S. W., Ahmad, Z., et al. (2006). MODIS land bands for ocean remote sensing applications. *Proc. Ocean Optics XVIII, Montreal, Canada*.

Gerace, A.D., Schott, J. R., & Nevins, R. (2013). Increased potential to monitor water quality in the near-shore environment with Landsat's next-generation satellite. *Journal of Applied Remote Sensing*, *7* 073558–073558.

Gohin, F. (2011). Annual cycles of chlorophyll-a, non-algal suspended particulate matter, and turbidity observed from space and in-situ in coastal waters. *Ocean Science*, *7*, 705–732.

Gordon, H. R., Brown, J. W., & Evans, R. H. (1988). Exact Rayleigh scattering calculations for use with the Nimbus-7 coastal zone color scanner. *Applied Optics*, *27*, 862–871.

Gordon, H. R., & Wang, M. (1994). Retrieval of water-leaving radiance and aerosol optical thickness over the oceans with SeaWiFS: A preliminary algorithm. *Applied Optics*, *33*, 443–452.

Gordon, H. R., & Wang, M. (1994). Influence of oceanic whitecaps on atmospheric correction of ocean-color sensors. *Applied Optics*, *33*, 7754–7763.

Govaerts, Y., & Clerici, M. (2004). *MSG-1/SEVIRI solar channels calibration commissioning activity report*. EUMETSAT (Doc EUM/MSG/TEN/04/2004).

Irons, J. R., Dwyer, J. L., & Barsi, J. A. (2012). The next Landsat satellite: The Landsat Data Continuity Mission. *Remote Sensing of Environment*, *122*, 11–21.

Kidwell, K. (1998). *NOAA Polar Orbiter Data User's Guide (TIROS-N, NOAA-6, NOAA-7, NOAA-8, NOAA-9, NOAA-10, NOAA-11, NOAA-12, NOAA-13 AND NOAA-14) November 1998 Revision*. NOAA/NESDIS/NCDC.

Kocum, E., Underwood, G. J., & Nedwell, D. B. (2002). Simultaneous measurement of phytoplanktonic primary production, nutrient and light availability along a turbid, eutrophic UK east coast estuary (the Colne Estuary). *Marine Ecology Progress Series*, *231*, 1–12.

Kou, L., Labrie, D., & Chylek, P. (1993). Refractive indices of water and ice in the 0.65-to 2.5-μm spectral range. *Applied Optics*, *32*, 3531–3540.

Kramer, H. J. (2002). *Observation of the earth and its environment: Survey of missions and sensors*. Springer.

Maes, J., Taillieu, A., Van Damme, P., Cottenie, K., & Ollevier, F. (1998). Seasonal patterns in the fish and crustacean community of a turbid temperate estuary (Zeeschelde Estuary, Belgium). *Estuarine, Coastal and Shelf Science*, *47*, 143–151.

Mertes, L. A., Smith, M.O., & Adams, J. B. (1993). Estimating suspended sediment concentrations in surface waters of the Amazon River wetlands from Landsat images. *Remote Sensing of Environment*, *43*, 281–301.

MTG Mission Requirement Document (2007). *EUM/MTG/SPE/06/0011*. EUMETSAT.

Nechad, B., Alvera-Azcaràte, A., Ruddick, K., & Greenwood, N. (2011). Reconstruction of MODIS total suspended matter time series maps by DINEOF and validation with autonomous platform data. *Ocean Dynamics*, *61*, 1205–1214.

Nechad, B., Ruddick, K., & Park, Y. (2010). Calibration and validation of a generic multisensor algorithm for mapping of total suspended matter in turbid waters. *Remote Sensing of Environment*, *114*, 854–866.

Neukermans, G., Ruddick, K., Bernard, E., Ramon, D., Nechad, B., Deschamps, P. -Y., et al. (2009). Mapping total suspended matter from geostationary satellites: A feasibility study with SEVIRI in the southern North Sea. *Optics Express*, *17*, 14029–14052.

Ouillon, S., Douillet, P., Petrenko, A., Neveux, J., Dupouy, C., Froidefond, J. -M., et al. (2008). Optical algorithms at satellite wavelengths for total suspended matter in tropical coastal waters. *Sensors*, *8*, 4165–4185.

Pahlevan, N., & Schott, J. R. (2013). Leveraging EO-1 to evaluate capability of new generation of Landsat sensors for coastal/inland water studies. *Sel. Top. Appl. Earth Obs. Remote Sens. IEEE J.*, *6*(2).

Pope, R. M., & Fry, E. S. (1997). Absorption spectrum (380–700 nm) of pure water. II. Integrating cavity measurements. *Applied Optics*, *36*, 8710–8723.

Rouse, L. J., & Coleman, J. M. (1976). Circulation observations in the Louisiana Bight using LANDSAT imagery. *Remote Sensing of Environment*, *5*, 55–66.

Ruddick, K., De Cauwer, V., Park, Y. -J., & Moore, G. (2006). Seaborne measurements of near infrared water-leaving reflectance: The similarity spectrum for turbid waters. *Limnology and Oceanography*, *51*, 1167–1179.

Ruddick, K. G., Ovidio, F., & Rijkeboer, M. (2000). Atmospheric correction of SeaWiFS imagery for turbid coastal and inland waters. *Applied Optics*, *39*, 897–912.

Smith, W. H., & Sandwell, D. T. (1997). Global sea floor topography from satellite altimetry and ship depth soundings. *Science*, *277*, 1956–1962.

Strod, T., Arad, Z., Izhaki, I., & Katzir, G. (2004). Cormorants keep their power: visual resolution in a pursuit-diving bird under amphibious and turbid conditions. *Current Biology*, *14*, R376–R377.

Stumpf, R. P., & Pennock, J. R. (1989). Calibration of a general optical equation for remote sensing of suspended sediments in a moderately turbid estuary. *Journal of Geophysical Research Oceans*, *1978–2012*(94), 14363–14371.

Thuillier, G., Hersé, M., Foujols, T., Peetermans, W., Gillotay, D., Simon, P., et al. (2003). The solar spectral irradiance from 200 to 2400 nm as measured by the SOLSPEC spectrometer from the ATLAS and EURECA missions. *Solar Physics*, *214*, 1–22.

United Kingdom Hydrographic Office (1985). *Admiralty tidal stream atlas and co-tidal charts Thames estuary NP249* (2nd ed.).

United Kingdom Hydrographic Office (1995). *Admiralty Tidal Stream Atlas Dover Strait NP233* (3rd ed.).

United Kingdom Hydrographic Office (2005). *Admiralty Tidal Stream Atlas North Sea Southern Part NP251* (4th ed.).

Utne-Palm, A. (2002). Visual feeding of fish in a turbid environment: Physical and behavioural aspects. *Marine and Freshwater Behaviour and Physiology*, *35*, 111–128.

Van der Woerd, H., & Pasterkamp, R. (2004). Mapping of the North Sea turbid coastal waters using SeaWiFS data. *Canadian Journal of Remote Sensing*, *30*, 44–53.

Vanhellemont, Q., Greenwood, N., & Ruddick, K. (2013). Validation of MERIS-derived turbidity and PAR attenuation using autonomous buoy data. *ESA Special Publication SP-722. Presented at the 2013 European Space Agency Living Planet Symposium, Edinburgh*.

Vanhellemont, Q., Neukermans, G., & Ruddick, K. (2013). Synergy between polar-orbiting and geostationary sensors: Remote sensing of the ocean at high spatial and high temporal resolution. *Remote Sensing of Environment*, http://dx.doi.org/10.1016/j.rse.2013.03.035.

Vanhellemont, Q., & Ruddick, K. (2011). Generalized satellite image processing: Eight years of ocean colour data for any region on earth. *Proc. SPIE 8175, Remote Sensing of the Ocean, Sea Ice, Coastal Waters, and Large Water Regions 2011* (pp. 81750Q).

Weiffen, M., Möller, B., Mauck, B., & Dehnhardt, G. (2006). Effect of water turbidity on the visual acuity of harbor seals (*Phoca vitulina*). *Vision Research*, *46*, 1777–1783.

Whitehouse, R. J., Harris, J. M., Sutherland, J., & Rees, J. (2011). The nature of scour development and scour protection at offshore windfarm foundations. *Marine Pollution Bulletin*, *62*, 73–88.

Wu, G., de Leeuw, J., Skidmore, A. K., Prins, H. H., & Liu, Y. (2007). Concurrent monitoring of vessels and water turbidity enhances the strength of evidence in remotely sensed dredging impact assessment. *Water Research*, *41*, 3271–3280.